

Proton capture strategy for enhancing electrochemical CO₂ reduction on atomically dispersed metal-nitrogen active sites

Xinyue Wang

Zhejiang University

Xiahan Sang

Wuhan University of Technology

Chung-Li Dong

Tamkang University

Siyu Yao

Zhejiang University

Ling Shuai

Central China Normal University

Jianguo Lu

Zhejiang University <https://orcid.org/0000-0001-6183-6336>

Bin Yang

Zhejiang University

Zhongjian Li

Zhejiang University

Lecheng Lei

Zhejiang University <https://orcid.org/0000-0002-4471-5898>

Ming Qiu

Central China Normal University

Liming Dai (✉ l.dai@unsw.edu.au)

University of New South Wales

Yang Hou

Zhejiang University

Article

Keywords: electrocatalysts, ECR, proton capture, water dissociation reaction

Posted Date: September 22nd, 2020

DOI: <https://doi.org/10.21203/rs.3.rs-73313/v1>

License:  This work is licensed under a Creative Commons Attribution 4.0 International License.

[Read Full License](#)

Abstract

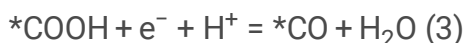
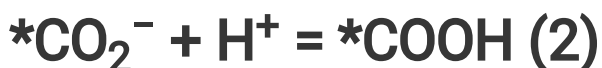
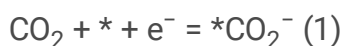
Electrocatalysts play a key role in accelerating the sluggish electrochemical CO₂ reduction (ECR) involving multi-electron and proton transfer. Herein, we develop a proton capture strategy via accelerating the water dissociation reaction catalyzed by transition metal nanoparticles (NPs) adjacent to atomically dispersed Ni-N_x active sites (Ni@NiNCM) to accelerate the proton transfer to the latter for boosting the intermediate protonation step, and hence the whole ECR process. For the first time, the accelerated protonation process is amply demonstrated experimentally. Aberration-corrected scanning transmission electron microscopy and synchrotron radiation X-ray absorption spectroscopy, together with DFT calculations, revealed that the Ni NPs accelerated the adsorbed H (H_{ad}) generation and transfer to the adjacent Ni-N_x sites for boosting the intermediate protonation and the overall ECR processes. This proton capture strategy is highly general, which can be extended to the design and preparation of various high-performance catalysts for diverse electrochemical reactions even beyond ECR.

Introduction

Electrochemical CO₂ reduction (ECR) has been widely studied as a mean of energy storage to tackle the current energy and environmental challenges¹. As a typical product that can be highly energy-efficiently generated through a two-electron transfer process, CO gas from ECR is very attractive for a wide range of industrial applications, including as an essential feedstock for Fischer-Tropsch synthesis^{2,3}. However, this technology still suffers multiple disadvantages, including the thermodynamic stability of CO₂, complex competitive reactions, and high-energy consumption. During the past few decades, significant efforts have been made to develop numerous chemically stable and earth-abundant metal-based electrocatalysts to facilitate ECR to CO, though rather limited progress was achieved.

Recently, transition metal (Fe, Co, Ni, etc.) and nitrogen co-doped carbon (TM-NC) based electrocatalysts were demonstrated to hold great potential as a class of efficient earth-abundant ECR catalysts⁴⁻⁷. It has been previously revealed that the delocalization of unpaired electron in 3*d* orbital to allow for efficient charge transfer from TM center to CO₂ molecule was beneficial to the activation of adsorbed CO₂ species and responsible for the high intrinsic ECR activity of TM-NC electrocatalysts⁵. Nevertheless, TM-NC catalysts still suffer from inefficient and sluggish reaction kinetics associated with the proton-coupled electron transfer process of CO₂ to CO⁸, which seriously hinder their practical applications.

It is well known that the CO production via ECR involves the following four key steps^{9,10}.





Among them, the protonation processes (Eqs. 2 and 3) with high energy barriers could significantly affect the reaction kinetics of ECR catalysis¹¹. In this regard, we envisioned that the protonation steps need to be optimized for an efficient proton capture in order to promote the formation of intermediates and CO. Thus, we propose to introduce TM nanoparticles (NPs)^{12,13}, especially Ni NPs, to promote the water dissociation and the formation of adsorbed hydrogen (H_{ad}) with a suitable binding energy for accelerating the protonation reaction kinetics¹⁴ – a possibility that has never been explored for ECR catalysis.

In this study, we developed a hybrid ECR electrocatalyst, composed of Ni NPs supported by a carbon matrix with atomically dispersed Ni-N_x sites (denoted as Ni@NiNCM), by a facile rotary evaporation, followed by calcination. The newly-developed Ni@NiNCM catalyst exhibited superior ECR performance with a maximum CO Faradic efficiency (FE) of ~ 97.6% and a low onset potential of -0.35 V, surpassing thus by far reported Ni single-atom catalysts (SACs), carbon-supported Ni NPs, and N-doped carbon ECR electrocatalysts. The improved ECR performance for the Ni@NiNCM catalyst was originated from synergistic effects between the atomic-level distribution of Ni-N_x active sites and Ni NPs attached on the carbon support, as evidenced by aberration-corrected scanning transmission electron microscopy (AC-STEM) and synchrotron radiation X-ray absorption spectroscopy (XAS) (*vide infra*). Density functional theory (DFT) calculations further demonstrated that Ni NPs could promote the adjacent atomic-level dispersed Ni-N_x active sites to capture protons from water dissociation catalyzed by the Ni NPs and significantly accelerate the transfer of H_{ad} to relevant ECR intermediates, consistent to the experimental observations. Moreover, a solar cell powered rechargeable Zn-CO₂ battery with a Ni@NiNCM cathode was assembled to demonstrate the production of CO from CO₂ via the ECR reaction (Eqs. 1–4).

Results And Discussion

Theoretical prediction of Ni@NiNCM model. We first performed computational studies to predict the rationally designed Ni@NiN_xCM architecture for boosting the catalytic activities. As previously reported^{5,15}, a NiN₄CM catalyst exhibited excellent electrocatalytic performance for CO₂-to-CO conversion, originating from the NiN₄CM's *d*-states that played an important role in the CO₂ activation and protonation processes^{16,17}. As such, one of the decisive steps to improve the intrinsic activity for boosting the ECR performance is to rationally modulate the *d*-states of the NiN₄CM catalyst. By analog, therefore, we optimized the geometric structure of Ni@NiN₄CM through the density of state calculations by CASTEP (Figs. 1a-1c). Figures 1d and 1e showed the partial density of states (PDOS) for Ni@NiN₄CM without and with adsorbed CO₂. As seen in Fig. 1d, the Ni@NiN₄CM model shows a strong peak of the highest occupied molecular orbital (HOMO) comprised of strengthened *d*-states from the Ni atoms¹⁸. Meanwhile, the states around the Fermi level indicate that the Ni@NiN₄CM model has a remarkable electron transport capability. These are two key factors for regulating the catalytic activities. As shown in Fig. 1e, the HOMO

peak of Ni@Ni₄CM downshifted only slightly compared with that in Fig. 1d, indicating that the active center and its electronic property could be well retained to show an excellent activity during the catalytic reactions.

Structural characterization of Ni@NiNCM. As schematically shown in Fig. 2a, the Ni@NiNCM was synthesized through N₂-protected carbonization of a precursor that was obtained via a simple rotary evaporation (42 °C) of an ethanol mixture solution of nickel nitrate (Ni(NO₃)₂·6H₂O) and o-phenylenediamine (oPD) ($W_{\text{Ni}}/W_{\text{oPD}}$ is 1/10). Possible effects of the carbonization temperature on the ECR performance of Ni@NiNCM were investigated in details over 700–1,000 °C, and the optimum temperature was found to be 900 °C (Supplementary Figs. 1–3).

Transmission electron microscopy (TEM) image of the as-prepared Ni@NiNCM shown in Fig. 2b displays a typical layered morphology characteristic of carbon nanosheets with the interspersed Ni NPs of ~ 15 nm in diameter. The corresponding high-resolution TEM (HRTEM) image shows an interplanar spacing of 2.0 Å, in consistent well with the (111) crystal plane of metallic Ni NPs (Fig. 2c). However, X-ray diffraction (XRD) pattern of Ni@NiNCM only exhibits a dominant peak around 27°, attributable to the graphitic carbon (Supplementary Fig. 4) with no metallic Ni peak^{19,20}, possibly due to the low content of Ni NPs while the Ni SACs are undetectable by XRD. The HRTEM examination of the carbon nanosheets free from Ni NPs reveals a mesoporous structure with a lattice distance of 3.4 Å, corresponding to the (002) facet of distorted graphitic carbon (Fig. 2d). The energy-dispersive X-ray spectroscopy (EDX) elemental mapping images of Ni@NiNCM show homogeneously distributed C, N, and Ni elements (Fig. 2e). Raman spectrum in Supplementary Fig. 5 displays three character peaks of D band (1,349 cm⁻¹), G band (1,583 cm⁻¹), and 2D band (2,650 cm⁻¹)^{21,22} with a I_D/I_G value of 1.01 for Ni@NiNCM, suggesting the existence of defects and/or disordered graphitic carbon structures associated with the N dopants and/or Ni NPs¹⁸.

X-ray photoelectron spectroscopy (XPS) analysis reveals the successful introduction of Ni, N, and C elements in Ni@NiNCM (Supplementary Fig. 6). Deconvoluted high resolution XPS N 1 s spectrum of Ni@NiNCM displays five typical peaks located at 398.2, 398.8, 399.7, 400.7, and 402.3 eV (Fig. 2f), attributable to pyridinic N, Ni-bonded N, pyrrolic N, graphitic N, and oxidized N, respectively. The high resolution XPS Ni 2p spectrum for Ni@NiNCM reveals the presence of metallic Ni⁰ (852.7 eV), Ni²⁺ (854.8 eV), and partially oxidized Ni³⁺ (855.8 eV)^{19,20} (Supplementary Fig. 7). The content of Ni species was determined to be 2.9 wt.% by inductively coupled plasma (ICP) analysis. Brunauer-Emmett-Teller (BET) measurements show a high BET surface area of 265 m² g⁻¹ for the porous structure of Ni@NiNCM, attractive for an efficient exposure of the catalytic active sites and a favorable transfer of the ECR-relevant species (Fig. 2g)^{21,22}.

ECR performance of Ni@NiNCM. The ECR activity of the Ni@NiNCM catalyst was evaluated in CO₂-saturated 0.5 M KHCO₃ electrolyte with three electrodes in an H-type cell. For comparison, ECR activity measurements were also performed on controlled samples of NiNCM prepared with sufficient acid

leaching to remove Ni NPs from of Ni@NiNCM, Ni NPs, and Ni NPs/NiNCM (physical mixture). Details of the preparation procedures (see details in Supporting Information) and structure characterization for these controlled samples are present in Supplementary Figs. 8–12. As shown in Fig. 3a, Ni@NiNCM displayed a marked increase in current density in the CO₂-saturated KHCO₃ electrolyte compared with the Ar-saturated KHCO₃, demonstrating the occurrence of ECR reaction under the CO₂-saturated condition. The onset potential of Ni@NiNCM for ECR was determined to be -0.35 V from CO generation revealed by the gas chromatography (GC) profile in Supplementary Fig. 13 while no any liquid product was detected by ¹H nuclear magnetic resonance (NMR) spectroscopy (Supplementary Fig. 14).

In order to evaluate the contribution of ECR catalysis to overall current density, the partial current densities of CO (j_{CO}) for the as-prepared catalysts were measured. As can be seen in Supplementary Fig. 15, the Ni NPs displayed a negligible activity for CO₂ reduction with j_{CO} of about 0.01 mA cm⁻². In contrast, NiNCM delivered a more favorable ECR activity with the maximum j_{CO} of 3.5 mA cm⁻² at a potential of -1.0 V. For Ni@NiNCM, the j_{CO} dramatically increased up to 13.5 mA cm⁻² at -1.0 V, indicating that Ni NPs in Ni@NiNCM significantly enhanced the ECR activity of NiNCM, though pure Ni NPs or Ni NPs physically mixed with NiNCM (i.e., Ni NPs/NiNCM with j_{CO} of 0.98 mA cm⁻²) displayed almost no activity for CO₂ reduction. Clearly, therefore, there is a strong synergistic effect between Ni NPs and NiNCM in the Ni@NiNCM catalyst. Among all the samples tested, Ni@NiNCM still exhibited the highest specific activity over the whole reduction potential even when the j_{CO} was normalized to per electrochemical double-layer capacitance (C_{dl}) (Fig. 3b and Supplementary Fig. 16). Moreover, CO FE of Ni@NiNCM could maintain over 90% under the potentials ranging from -0.7 V to -1.1 V, with the maximum CO FE of 97.6% at -0.9 V, while the CO FEs of NiNCM, Ni NPs, and Ni NPs/NiNCM were only 73.0%, 17.0%, and 21.1%, respectively, at -0.9 V (Fig. 3c). Notably, the observed high ECR performance of Ni@NiNCM exceeded that of almost all previously-reported benchmarking ECR electrocatalysts based on N-doped carbon, Ni SAC, and carbon-supported Ni NPs reported to date (Fig. 3d and Supplementary Table 1). The superb ECR performance of Ni@NiNCM was further supported by its turnover frequency (TOF) up to 839 h⁻¹ at -0.9 V (Supplementary Fig. 17 and Supplementary Table 2), a value which is almost two times higher than that of NiNCM (465 h⁻¹) and also superior to that of Ni NPs (25 h⁻¹).

To gain the insight of reaction kinetics, we obtained a Tafel slope of 90 mV dec⁻¹ for NiNCM, which is between 120 mV dec⁻¹ (Eqs. 1) and 60 mV dec⁻¹ (Eq. 2) and indicate that the *CO₂⁻ generation and the subsequent protonation reaction have a crucial effect on ECR process²³. Compared with NiNCM, Ni@NiNCM showed a markedly decreased Tafel slope (52 mV dec⁻¹, Fig. 3e), indicating that the protonation step was significantly improved by Ni NPs in the Ni@NiNCM due to an enhanced proton capture. This is further supported by electrochemical impedance spectra (EIS) shown in Supplementary Fig. 18, in which Ni@NiNCM showed a smaller impedance, and hence the faster electron transfer than that of NiNCM and Ni NPs.

To evaluate the long-term stability, we tested simultaneously both the electrochemical stability and performance stability of Ni@NiNCM. As shown in Fig. 3f, the CO FE could maintain over 90% with the current density declined only by ~ 9% after 10-hours electrocatalysis. After the long-term testing, the morphology and chemical structure of Ni@NiNCM were found to be well-preserved from the post-test sample characterization by various microscopic and spectroscopic techniques, including TEM, XRD, and XPS. Clearly, therefore, Ni@NiNCM is highly stable under the ECR conditions (Supplementary Figs. 19–21).

Identification of active sites. In order to reveal the local chemical coordination environments of Ni@NiNCM, we further performed XAS measurements. The Ni K-edge X-ray adsorption fine structure (XANES) spectra show that the pre-edge of Ni@NiNCM is between NiO and Ni foil (Fig. 4a), indicating that the average valance of Ni species in the Ni@NiNCM is at a partially oxidized state. This is consistent well with the height of the white-line peak marked by dark red circle. Considering that the valance of the Ni NPs is zero, the higher oxidation state implies the existence of another coordination form of Ni atoms except the Ni NPs in Ni@NiNCM. The Fourier transforms of extended X-ray absorption fine structure (EXAFS) (R-space, Fig. 4b) for Ni@NiNCM displays a dominant peak similar to that of the Ni foil, corresponding to the Ni-Ni scattering path. The frontal position of Ni@NiNCM was offset to 2.1 Å, while that of the Ni foil was located at 2.2 Å, indicating that the Ni-Ni bond in the Ni@NiNCM was slightly shorter than that of the Ni foil. Interestingly, a slight acromion was observed for Ni@NiNCM referring to the Ni-N bonding of nickel phthalocyanine (NiPc), as marked by the light green shadow. Although the characteristic peak of Ni-N bonds was suppressed by the dominant peak of Ni-Ni in Ni NPs, the existence of Ni-N_x bonds in Ni@NiNCM could still be evident²⁴, which was further supported by EXAFS fitting results in Supplementary Fig. S22 and Table 3. To obtain more precise information on the coordination environments of Ni species throughout the whole Ni@NiNCM catalyst sample, we applied the continuous wavelet transform (WT) to the EXAFS spectra (Fig. 4c). Compared with that of the Ni foil, the WT contour plot of Ni@NiNCM significantly shifted to the negative side due to the Ni-N_x contributions, further verifying the coordination of Ni and N. Impressively, the coexistence of the Ni-N_x coordination with Ni NPs attached on the carbon matrix could be directly observed by AC-STEM with EDX element mapping (Fig. 4d). The signals of Ni element in the EDX element mapping images could not only be clearly seen over the Ni NPs but also to be dispersed uniformly together with N element in the carbon matrix²⁵, demonstrating that the Ni-N_x species were anchored around the Ni NPs. Furthermore, these atomic-level Ni sites around the Ni NPs could be clearly identified by atomic-resolution high-angle annular dark-field (HAADF) analysis, as shown in Figs. 4e and 4 f. The bright dots marked by yellow circles showed a distinctly different contrast with a diameter of ~ 0.22 nm corresponding to isolated Ni atoms. Thus, the above results clearly revealed that the atomic-level Ni-N_x sites anchored around Ni NPs on the carbon matrix.

To further verify the active sites, we used SCN⁻ ions, as a remarkable catalytic activity inhibitor²⁶, to block the atomic-level dispersed Ni-N_x sites in Ni@NiNCM. It was observed that the maximum CO FEs of Ni@NiNCM and NiNCM reduced from 97.6–71.9% (Fig. 4g and Supplementary Fig. 23) and from 73.0–

51.9% (Supplementary Fig. 24), respectively, but not for the bare Ni NPs (Supplementary Fig. 25), upon the introduction of SCN^- ions. These results revealed that the Ni-N_x sites played a significant role for the CO production during the ECR process, while the Ni NPs only accelerated reaction kinetics by boosting the protonation procedure (Eqs. 3 and 4, see above).

To obtain insights into the role of Ni NPs in accelerating protonation during the ECR process, we have conducted studies on the kinetic isotope effect (KIE) of H/D ($\text{H}_2\text{O}/\text{D}_2\text{O}$) over the Ni@NiNCM and NiNCM catalysts. The KIE can be used as an indicator of the proton transfer rate of water dissociation, which is the major proton donor for the ECR protonation process²⁷. The KIE of NiNCM was calculated to be 2.45, while the KIE value over the Ni@NiNCM sharply decreased to 1.24. This result reveals that the introduced Ni NPs in the Ni@NiNCM is responsible for the dissociation of water to accelerate the proton transfer process (Supplementary Fig. 26a).

To gain further evidence for the role of Ni NPs, we have investigated the effect of local pH change that may contribute to the enhanced ECR performance. As such, three different electrolytes were used to adjust the local pH environment at the cathode/electrolyte interface with the following sequence: $\text{K}_2\text{HPO}_4 < \text{K}_2\text{CO}_3 < \text{K}_2\text{SO}_4$ ²⁸. The electrochemical results showed that the formation rate of CO product over both Ni@NiNCM and NiNCM catalysts increased in the same order of $\text{K}_2\text{HPO}_4 < \text{K}_2\text{CO}_3 < \text{K}_2\text{SO}_4$ (Supplementary Fig. 26b). However, the increased ratio of CO production rate for Ni@NiNCM and NiNCM (donated as $\text{Rate}_{\text{Ni@NiNCM}}/\text{Rate}_{\text{NiNCM}}$ ratio) in K_2SO_4 (2.66) is higher than those of in K_2HPO_4 (2.10) and K_2CO_3 (2.55) (Supplementary Fig. 26c). This observation demonstrates that the presence of Ni NPs accounts for the promoted CO production by accelerating the water dissociation process, although the dissociation of water becomes more difficult at a higher pH^{29,30}. Furthermore, it was observed that the enhancement in the CO promotion rate over NiNCM was very limited with respect to that of Ni@NiNCM, further confirming the positive role of Ni NPs enhancing the dissociation of water to boost the proton transfer process.

DFT calculations. For clarifying the intrinsic ECR mechanism, we have constructed four different models based on the XAS results. These models are consisting of the NiN₁, NiN₂, NiN₃, and NiN₄ coordinated structures anchored adjacent to Ni NPs on the carbon matrix, which are donated as Ni@NiN₁CM, Ni@NiN₂CM, Ni@NiN₃CM, and Ni@NiN₄CM, respectively. As shown in Figs. 5a-5c, the detailed reaction pathways of CO₂ transition to CO, hydrogen evolution traction (HER), and water dissociation in a weak alkaline solution (pH = 7.2) were calculated for those models. In Fig. 5a, the pathways for CO₂ adsorption and CO desorption are almost up-hilled, indicating the needs of external potentials to drive the endothermic reactions. The free energies of CO₂ adsorption for Ni@NiN₁CM, Ni@NiN₂CM, and Ni@NiN₃CM models are 2.409, 2.713, and 3.389 eV (U = 0 V), respectively, while it is about 0.000 eV for Ni@NiN₄CM. The NiN₄ structure has been previously demonstrated to capture CO₂ molecules³¹, while the Ni NPs could synergistically work for HER process³² which is in favor of adsorbing the H_{ad} and facilitates the protonation process of ECR. As such, the Ni NPs deposited on the carbon matrix can modify the

electronic structures of adjacent NiN₄ centers to form an interactive active center for CO₂ reduction (Fig. 5a). For desorption of CO, the free energies are 2.866, 0.598, 2.290, and 2.567 eV for Ni@NiN₁CM, Ni@NiN₂CM, Ni@NiN₃CM, and Ni@NiN₄CM, respectively. The above four models display strong bonding forces of *CO intermediate on the active centers, indicating that the *COOH transition to *CO can be accelerated by the short bond length. The overpotentials of ECR process were calculated to be 2.866, 3.389, 2.713, and 2.567 eV for Ni@NiN₁CM, Ni@NiN₂CM, Ni@NiN₃CM, and Ni@NiN₄CM, respectively. These DFT results combined with the above PDOS calculations (Figs. 1d and 1e) reveal that the excellent electron transport and capture capacity of H_{ad} for the Ni@NiN₄CM model leads to a significant decrease in the potential barrier for CO₂ activation.

Figures 5b and 5c show the reaction pathway profiles for HER and water dissociation processes associated with these four models. As can be seen in Fig. 5b, the HER overpotentials are 1.755, 2.311, 2.151, and 0.746 eV for Ni@NiN₁CM, Ni@NiN₂CM, Ni@NiN₃CM, and Ni@NiN₄CM, respectively. Figure 5c shows the lowest free energy of 0.048 eV for Ni@NiN₄CM during the water dissociation process. The weakened free energy for water dissociation can help to accelerate the H₂O transition to H_{ad}, thus effectively capturing protons to boost the ECR reaction kinetics. In addition, the free energies of NiN₄ model with *CO₂, *COOH, and *CO intermediates are presented in Supplementary Fig. 27. These results indicate that Ni NPs can facilitate protons transport from the Ni NPs to NiN₄ centers to form the intermediates, thus speeding up the whole ECR process. From Fig. 5d, it can be seen that the Ni NP can assist to capture H₂O and H_{ad}, thus promoting the *CO₂ transition to *COOH on the Ni atom in the NiN₄ structure, and the proposed reaction mechanism is shown in Fig. 5e. Consequently, the surface state hybridization induced by the Ni NPs on NiN₄ cause a change in the adsorption strengths of intermediates and potential barriers for certain elementary steps of ECR, which optimizes the reaction kinetics and boosts the ECR catalytic activities.

Zn-CO₂ battery. To demonstrate the ECR catalysts for potential applications, we developed an integrated Zn-CO₂ battery based on the Ni@NiNCM cathode. A Zn-CO₂ battery can safely convert CO₂ into green chemical fuels and clean electricity. Figure 6a shows a schematic diagram of the Zn-CO₂ battery developed in this study, in which the Ni@NiNCM was used as a cathode for efficient reducing CO₂ to CO (also, NiNCM or Ni NPs/NiNCM was used for comparison) with Zn plate as the anode. Figure 6b shows the charge-discharge voltage profiles of the Zn-CO₂ battery, along with the polarization curves for the anodic oxygen evolution of the Ni@NiNCM, NiNCM, and Ni NPs/NiNCM electrodes in Supplementary Fig. 28³³⁻³⁵. The power density of Ni@NiNCM was further calculated in Fig. 6c with a maximum value up to 1.0 mW cm⁻², which was much higher than that of NiNCM and Ni NPs/NiNCM. For discharge processes at different constant current densities (Fig. 6d), Ni@NiNCM displayed the higher discharge capacity, delivering a stable current of 1.0 mA cm⁻² at 0.22 V, along with an energy density of 386 Wh kg⁻¹. Figure 6e shows the galvanostatic discharge-charge cycling curve for the Zn-CO₂ based on the Ni@NiNCM cathode at 1.0 mA cm⁻² for 90 circles (32 h), indicating a good durability. In addition, three

Ni@NiNCM based Zn-CO₂ batteries were put into series to light up a LED bulb (Fig. 6f). Furthermore, we have also successfully demonstrated the feasibility to use an integrated solar panel to recharge the Zn-CO₂ battery (Figs. 6g and 6 h).

Discussion

As can be seen from above, we have developed a proton capture strategy by hybridizing Ni NPs with atomically dispersed Ni-N_x species on a carbon matrix to enhance the H_{ad} capture for the protonation intermediate step, and hence the whole ECR process. The newly-developed Ni@NiNCM catalyst exhibited a prominent ECR activity with the maximum CO FE of around 97.6% at -0.9 V and a low onset potential of -0.35 V, ranking top in all previously-reported Ni SAC, carbon-supported Ni NPs, and N-doped carbon materials. This proton capture strategy is highly general, which could be further extended to develop other NPs@TM-NC catalysts as the Ni NPs can be hybridized with TM porphyrin series that possess internal TM center coordinated with four N atoms structure (TM-N₄). Our preliminary results confirmed that the ECR activities of TM-N₄ (e.g., FePc/C, CoPc/C) can indeed be improved by hybridizing with Ni NPs (Supplementary Fig. 29). Our microscopic and spectroscopic results revealed that the Ni NPs located adjacent to the atomically dispersed Ni-N_x species while the DFT calculations demonstrated that Ni NPs adjacent to the NiN₄ centers could enhance the *d* state contribution of the NiN₄ moieties and accelerate the proton transport to ECR intermediates to boost the overall ECR activity, in agreement with experiments. The combined experimental and calculation results are promising and promoted us to construct Zn-CO₂ battery with the Ni@NiNCM cathode for CO₂ conversion with the highest power density of 1.0 mW cm⁻² and three of such Zn-CO₂ batteries in series could light up a LED bulb. Also, we have successfully integrated a solar cell to recharge the Zn-CO₂ battery with a Ni@NiNCM cathode. The proton capture strategy developed in this work is highly general and can be used to guide the design and preparation of various high-performance catalysts for diverse electrochemical reactions, such as hydrogen evolution, carbon monoxide reduction, and nitrogen reduction reactions.

Methods

Synthesis of Ni@NiNCM. In a typical experiment, 0.2477 g of Ni(NO₃)₂·6H₂O and 0.5 g of oPD were dissolved in 80 mL of ethanol under moderately stirring (50 rpm) at room temperature for 30 min. Then, the ethanol solvent was removed by rotary evaporation (IKA RV 10) to obtained powder product, followed by carbonization at 900 °C for 2 h under N₂ atmosphere. Finally, the carbonized product was leached in 0.5 M H₂SO₄ at 90 °C for 4 h to remove unstable metallic Ni species and NiO.

Characterization. The morphologies of the as-prepared samples were characterized by field emission scanning electron microscopy (FESEM) (SU8010), and TEM (JEOL-2100F), and HRTEM (Tecnai G2 F20S-TWIN) as well as AC-STEM imaging (Titan Cubed Themis G2 300). The Ni element content was measured by ICP analysis (730-ES). Raman spectroscopy was performed on Laser confocal Raman

spectrometer (LabRAM HR Evolution). The crystallization degree was examined using a ZETIUM DY powder XRD with Cu K α X-rays at 4 KW. The XPS measurements was done by using an Escalab 250Xi system equipped with a microfocusing monochromatic Al K α source and high region resolution up to 0.45 eV. The BET surface area was measured on AUTOSORB-IQ-MP at 77 K. XAS data were collected at BL14W1 beamline in Shanghai Synchrotron Radiation Facility (SSRF) and Beijing Synchrotron Radiation Facility (BSRF). The storage ring of SSRF was operated at 3.5 GeV with a maximum current of 240 mA. Using a Si (111) double-crystal monochromator, the Ni K-edge data collection was carried out in the fluorescence mode with a Lytle detector full of argon gas.

Electrochemical measurements. ECR test was performed on a three-electrode system in a H-type cell. The Ni@NiNCM catalyst was used as the working electrode with Ag/AgCl as the reference electrode, which were placed in cathode chamber, while the Pt gauze was served as the counter electrode in the anode side. Two electrolytes were separated by a Nafion 117 membrane to ensure the proton exchange and to avoid the electrolyte crossover contamination. Before the electrochemical testing, the cell was bubbled with CO₂ flow at 20 mL min⁻¹ for 30 min. Then, the polarization curves were recorded over potential ranges from 0 V to -1.2 V (vs. RHE) with a scan rate of 5 mV s⁻¹. The polarization curves were further collected after cyclic voltammograms (CV) activation over the same potential windows. The CV curves used for the ECSA calculations were scanned from 0.44 V to 0.54 V (vs. RHE). The EIS measurements were carried out by applying -0.5 V (vs. RHE) with 100 mV amplitude in a frequency range from 100 KHz to 100 mHz. In this work, on-line GC and off-line ¹H NMR measurements were applied for analyzing the gaseous and liquid products and their FEs at different applied potentials.

Computational details. DFT calculations were conducted in Material Studio using the Cambridge Serial Total Energy Package (CASTEP), which is based on the DFT plane-wave pseudopotential approach. See more details in the Supporting Information.

Data Availability

The data that support the findings of this study are available from the corresponding author upon reasonable request.

Declarations

Competing interests

The authors declare no competing interests.

Author contributions

X.W. L.D., and Y.H. conceived the idea and performed the experiments. C.D. and S.Y. collected and analyzed the XAS data. X.S. performed the AC-STEM characterizations. M.Q. and S.L. conducted and discussed the DFT calculations. J.L., B.Y., Z.L., and L.L. provided helpful suggestions. X.W., Y.H., M.Q., and L.D. wrote the manuscript. All authors discussed the results and commented on the manuscript.

Acknowledgments

Y.H. acknowledges great support of the National Natural Science Foundation of China (21922811, 51702284, 21878270, and 21961160742), Zhejiang Provincial Natural Science Foundation of China (LR19B060002), the Fundamental Research Funds for the Central Universities, the Startup Foundation for Hundred-Talent Program of Zhejiang University, and the Leading Innovative and Entrepreneur Team Introduction Program of Zhejiang (2019R01006). M. Qiu acknowledges the support of Hubei Natural Science Foundation of China (2018CFB531). L. Dai is grateful for the partial support by ARC (DP 190103881 and FL 190100126).

Correspondence and requests for materials should be addressed to Y.H., M.Q., and L.D. (Email: yhou@zju.edu.cn; qium@mail.ccnu.edu.cn; l.dai@unsw.edu.au).

Reprints and permissions information is available at www.nature.com/reprints.

References

1. Liu, M. et al. Enhanced electrocatalytic CO₂ reduction via field-induced reagent concentration. *Nature* **537**, 382–386 (2016).
2. Ma, T. et al. Heterogeneous electrochemical CO₂ reduction using nonmetallic carbon-based catalysts: current status and future challenges. *Nanotechnology* **28**, 472001 (2017).
3. Wang, Y. et al. Efficient solar-driven electrocatalytic CO₂ reduction in a redox-medium-assisted system. *Nat. Commun.* **9**, 5003 (2018).
4. Wang, T. et al. Carbon-Rich Nonprecious Metal Single Atom Electrocatalysts for CO₂ Reduction and Hydrogen Evolution. *Small Methods* **3**, 1900210, (2019).
5. Yang, H. et al. Atomically dispersed Ni(I) as the active site for electrochemical CO₂ reduction. *Nat. Energy* **3**, 140–147 (2018).
6. Lin, L. et al. Synergistic Catalysis over Iron-Nitrogen Sites Anchored with Cobalt Phthalocyanine for Efficient CO₂ Electroreduction. *Adv. Mater.* **31**, 1903470 (2019).
7. Wang, X. et al. Emerging Nanostructured Carbon-based Non-precious Metal Electrocatalysts for Selectively Electrochemical CO₂ Reduction to CO. *J. Mater. Chem. A* **7**, 25191–25202 (2019).
8. Sun, D. & Chen, Y. Electrochemical Energy Storage and Conversion: Fundamentals and Technologies. Boca Raton, Florida: *CRC Press* (2016).

9. Rong, X. et al. Control Synthesis of Vacancy-Defect Single-Atom Catalyst for Boosting CO₂ Electroreduction. *Angew. Chem. Int. Ed.* **59**, 1961–1965 (2019).
10. Möller, T. et al. Efficient CO₂ to CO electrolysis on solid Ni-N-C catalysts at industrial current densities. *Energy Environ. Sci.* **12**, 640–647 (2019).
11. Schoeberger, W. et al. Electrocatalytic Reduction of CO₂ to Acetic Acid by a Molecular Manganese Corrole Complex. *Angew. Chem. Int. Ed.* **59**, 10527–10534 (2020).
12. Lei, C. et al. Efficient alkaline hydrogen evolution on atomically dispersed Ni-N_x Species anchored porous carbon with embedded Ni nanoparticles by accelerating water dissociation kinetics. *Energy Environ. Sci.* **12**, 149–156 (2019).
13. Tiwari, J. et al. High-Performance Hydrogen Evolution by Ru Single Atoms and Nitrided-Ru Nanoparticles Implanted on N-Doped Graphitic Sheet. *Adv. Energy Mater.* **9**, 1900931 (2019).
14. Frese, K. Calculation of surface binding energy for hydrogen, oxygen, and carbon atoms on metallic surfaces. *Surf. Sci.* **182**, 85–97 (1987).
15. Li, X. et al. Exclusive Ni-N₄ Sites Realize Near-Unity CO Selectivity for Electrochemical CO₂ Reduction. *J. Am. Chem. Soc.* **139**, 14889–14892 (2017).
16. Schneider, J. et al. Thermodynamics and kinetics of CO₂, CO, and H⁺ binding to the metal centre of CO₂ reduction catalysts. *Chem. Soc. Rev.* **41**, 2036–2051 (2012).
17. Lin, W. et al. Mechanisms of Hydrogen-Assisted CO₂ Reduction on Nickel. *J. Am. Chem. Soc.* **139**, 4663–4666 (2017).
18. Liu, B. et al. Atomically Dispersed Ni(I) on Alloy-Encapsulated Nitrogen-Doped Carbon Nanotube Array for High-Performance Electrochemical CO₂ Reduction Reaction. *Angew. Chem. Int. Ed.* **59**, 12055–12061 (2020).
19. Yan, C. et al. Coordinatively unsaturated nickel-nitrogen sites towards selective and high-rate CO₂ electroreduction. *Energy Environ. Sci.* **11**, 1204–1210 (2018).
20. Xiong, W. et al. CuSn Alloy Nanoparticles on Nitrogen-Doped Graphene for Electrocatalytic CO. *ChemElectroChem* **6**, 5951–5957 (2019).
21. Zheng, W. et al. Atomically Defined Undercoordinated Active Sites for Highly Efficient CO₂ Electroreduction. *Adv. Funct. Mater.* **30**, 1907658 (2019).
22. He, Y. et al. Porous carbon nanosheets: Synthetic strategies and electrochemical energy related applications. *Nano Today* **24**, 103–119 (2019).
23. Zheng, W. et al. Highly active metallic nickel sites confined in N-doped carbon nanotubes toward significantly enhanced activity of CO₂ electroreduction. *Carbon* **150**, 52–59, (2019).
24. Chen, M. et al. Identification of Catalytic Sites for Oxygen Reduction in Metal/Nitrogen-Doped Carbons with Encapsulated Metal Nanoparticles. *Angew. Chem. Int. Ed.* **59**, 1627–1633 (2020).
25. Pan, F. et al. Boosting CO₂ reduction on Fe-N-C with sulfur incorporation: Synergistic electronic and structural engineering. *Nano Energy* **68**, 104384 (2020).

26. Pan, F. et al. Atomic-level active sites of efficient imidazolate framework-derived nickel catalysts for CO₂ reduction. *J. Mater. Chem. A* **7**, 26231–26237 (2019).
27. German, E. D. & Sheintuch, M. Quantum effects in the kinetics of H₂O dissociative adsorption on Pt(111), Cu(111), Rh(111), and Ni(111). *J. Phys. Chem. C* **114**, 3089–3097 (2010).
28. Hori, Y., Murata, A. & Takahashi, R. Formation of hydrocarbons in the electrochemical reduction of carbon dioxide at a copper electrode in aqueous solution. *J. Chem. Soc. Faraday Trans.* **85**, 2309–2326 (1989).
29. Ma, W. et al. Promoting electrocatalytic CO₂ reduction to formate via sulfur-boosting water activation on indium surfaces. *Nat. Commun.* **10**, 892 (2019).
30. Ma, W. et al. Electrocatalytic reduction of CO₂ to ethylene and ethanol through hydrogen-assisted C–C coupling over fluorine-modified copper. *Nat. Catal.* **3**, 478–487 (2020).
31. Lu, C. et al. Atomic Ni Anchored Covalent Triazine Framework as High Efficient Electrocatalyst for Carbon Dioxide Conversion. *Adv. Funct. Mater.* **29**, 1806884 (2019).
32. Gong, M. et al. Nanoscale nickel oxide/nickel heterostructures for active hydrogen evolution electrocatalysis. *Nat. Commun.* **5**, 4695 (2014).
33. Lei, C. et al. Fe-N₄ Sites Embedded into Carbon Nanofiber Integrated with Electrochemically Exfoliated Graphene for Oxygen Evolution in Acidic Medium. *Adv. Energy Mater.* **8**, 1801912 (2018).
34. Hou, Y. et al. Atomically dispersed nickel-nitrogen-sulfur species anchored on porous carbon nanosheets for efficient water oxidation. *Nat. Commun.* **10**, 1392 (2019).
35. Cheng, X. et al. A strongly coupled 3D ternary Fe₂O₃@Ni₂P/Ni(PO₃)₂ hybrid for enhanced electrocatalytic oxygen evolution at ultra-high current densities. *J. Mater. Chem. A* **7**, 965–971 (2019).

Figures

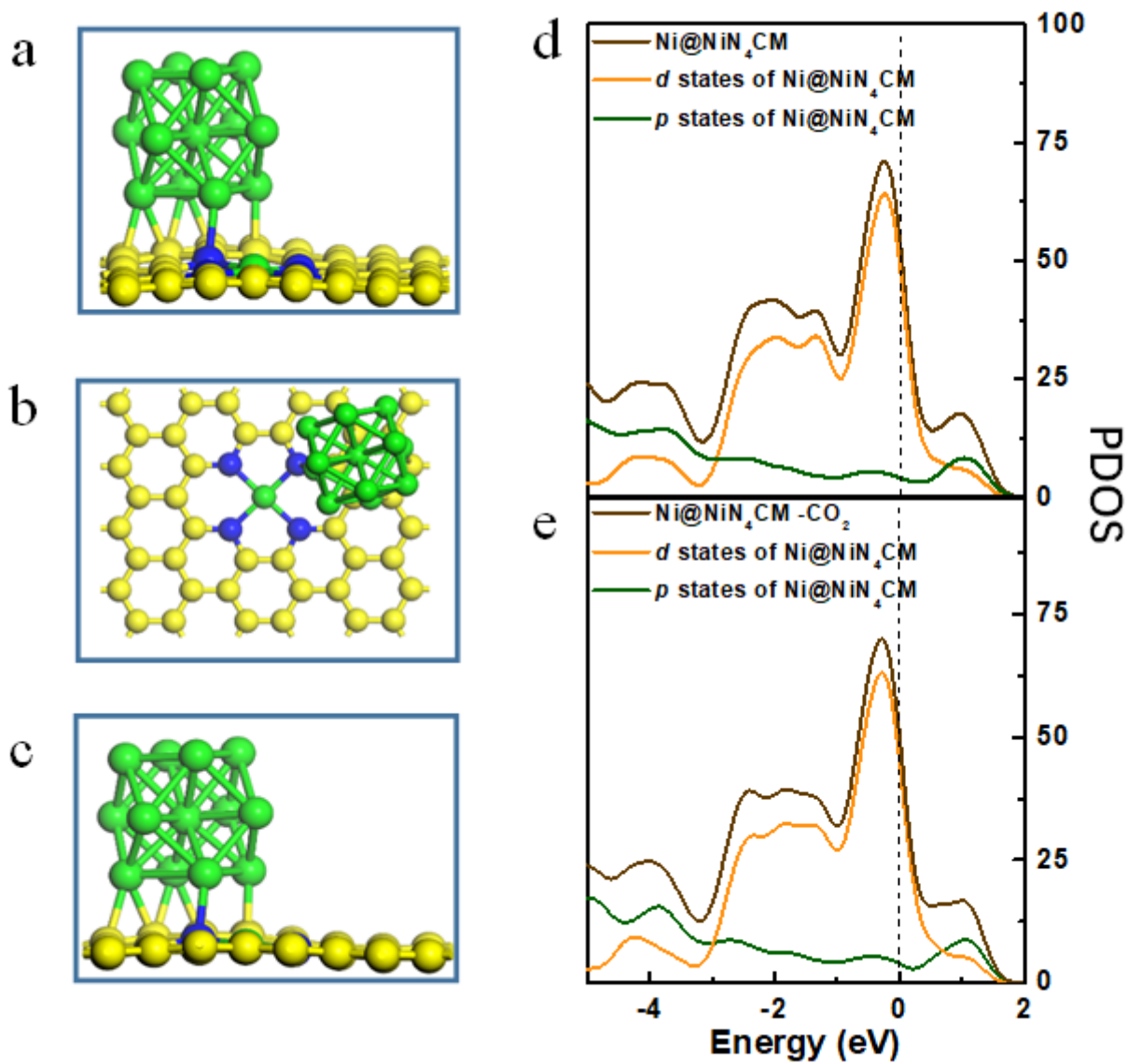


Figure 1

Theoretical prediction of Ni@NiNCM model. Schematic diagrams of Ni@Ni₄CM model: a, Side view, b, Top view, c, Front view. PDOS of Ni atom in optimized structures for Ni@Ni₄CM without d, and with CO₂ adsorbed e.

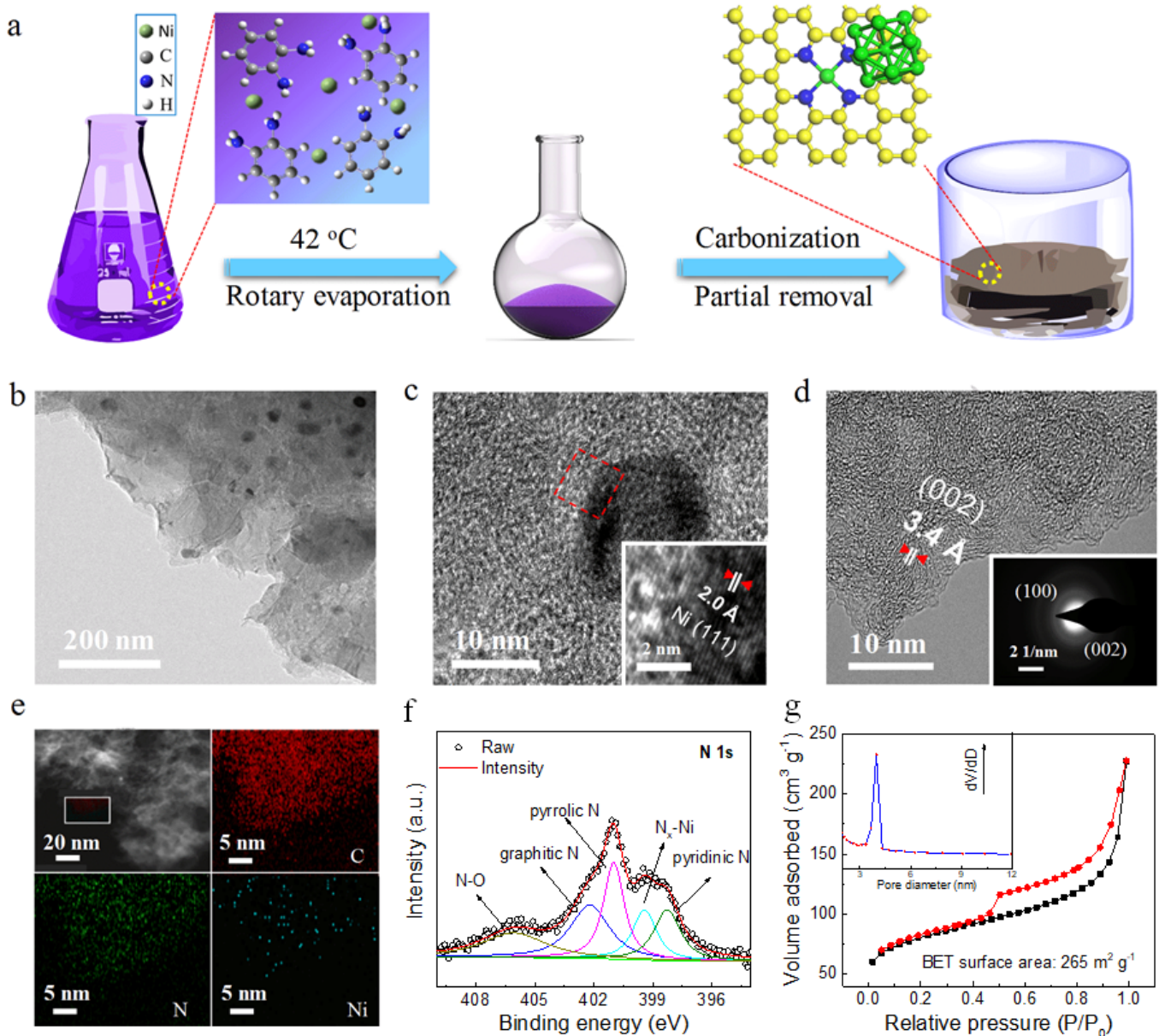


Figure 2

Structural characterizations of Ni@NiNCM. a, Schematic illustration of synthesis process, b, TEM image, c, HRTEM image of embedded Ni NPs. Inset: enlarged HRTEM image of the red rectangle, d, HRTEM image of porous carbon nanosheets without Ni NPs. Inset: SAED pattern, e, EDX element mappings images of C, N, and Ni elements. f, High resolution XPS N 1s spectrum, g, N₂ adsorption-desorption isotherm curve of Ni@NiNCM. Inset in g: corresponding distribution of pore size.

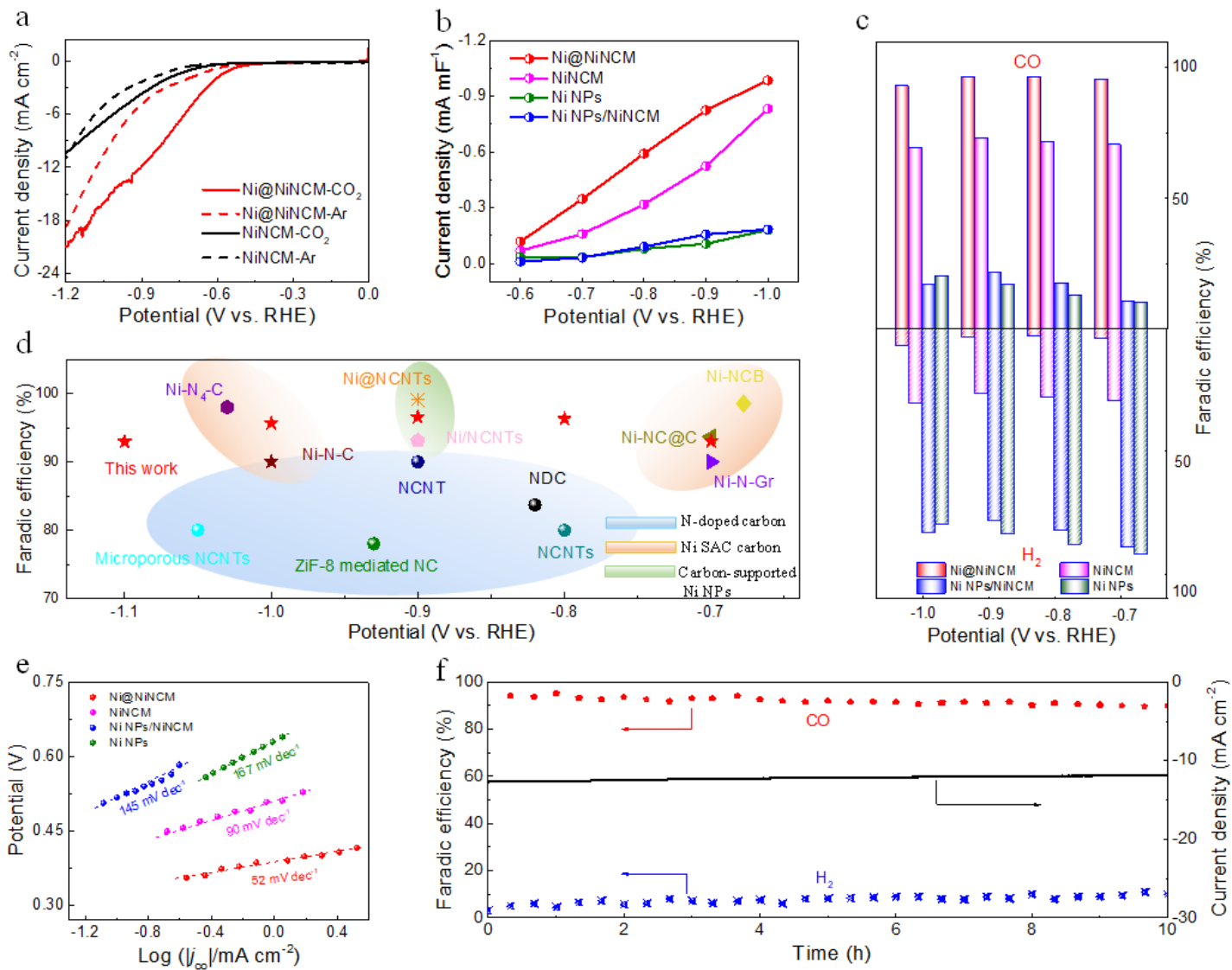


Figure 3

ECR performances of Ni@NiNCM. a, Polarization curves of Ni@NiNCM (red solid) and NiNCM (black solid) in CO₂-saturated 0.5 M KHCO₃ solution and the dotted lines were in Ar-saturated 0.5 M KHCO₃ solution. b, Normalized CO partial current densities to CdI. c, FEs of CO and H₂ products at different applied potentials, d, the maximum CO FE of Ni@NiNCM compared with other reported ECR electrocatalysts based on N-doped carbon, Ni SAC carbon, and carbon-supported Ni NPs. e, Corresponding Tafel slopes. f, Potentiostatic curve for 10 hours at -0.9 V with CO and H₂ FEs during long-time electrocatalysis.

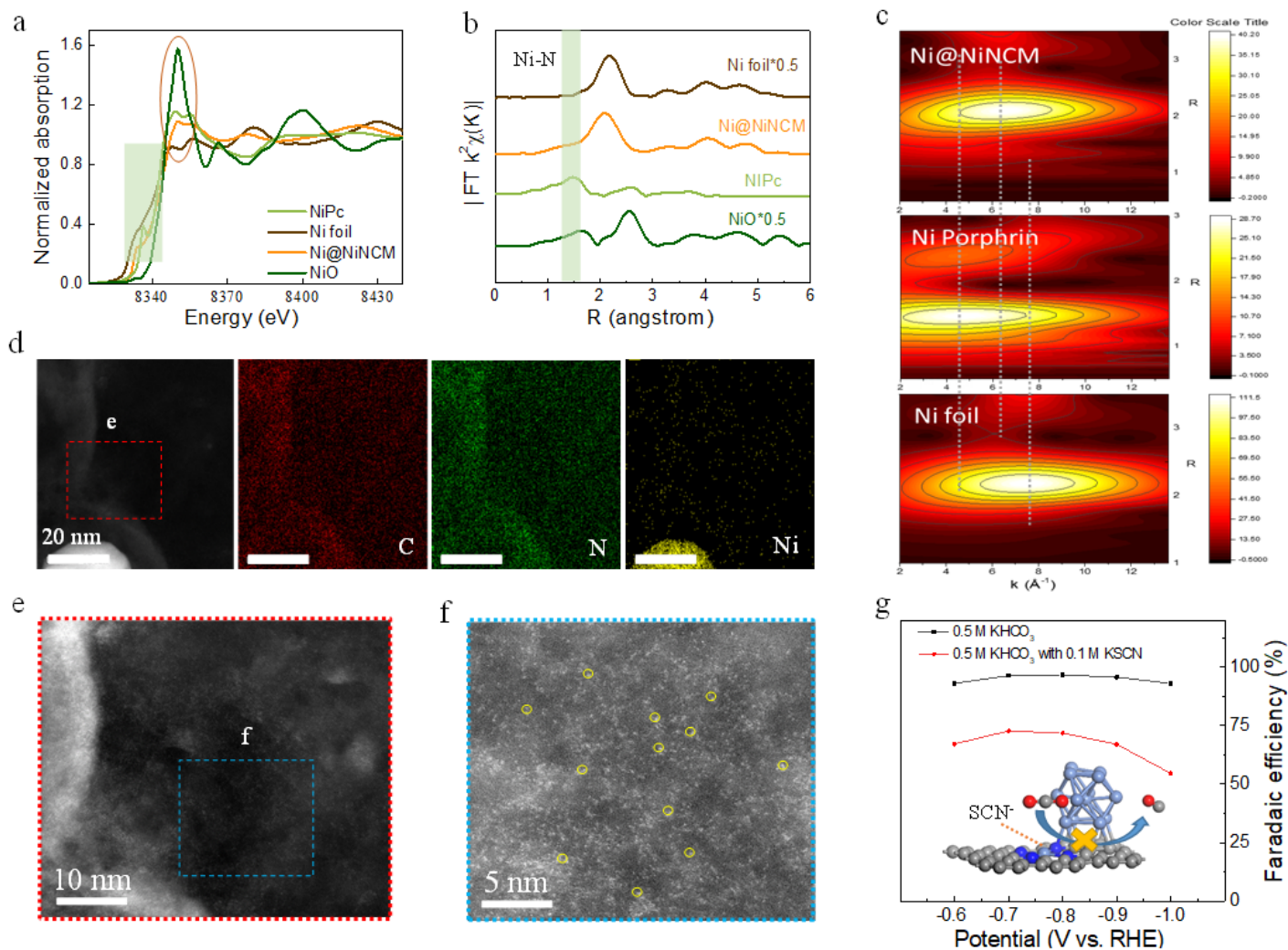


Figure 4

Understanding active sites of Ni@NiNCM. a, Ni K-edge XANES and b, EXAFS spectra of Ni@NiNCM with reference samples of Ni foil, NiO, and NiPc, and c, WT-EXANES spectra of Ni@NiNCM compared with Ni foil and NiPc. d, EDX element mappings images of C, N, and Ni elements at surrounding region of escaped Ni NPs. e, AC-STEM image of the region in d. f, enlarged image of e, atomic-level Ni species displaying in form of the bright dots highlighted by yellow circles. g, CO FEs of Ni@NiNCM with and without 0.1 M SCN⁻ ions. Inset: illustrations of proposed poisoning model.

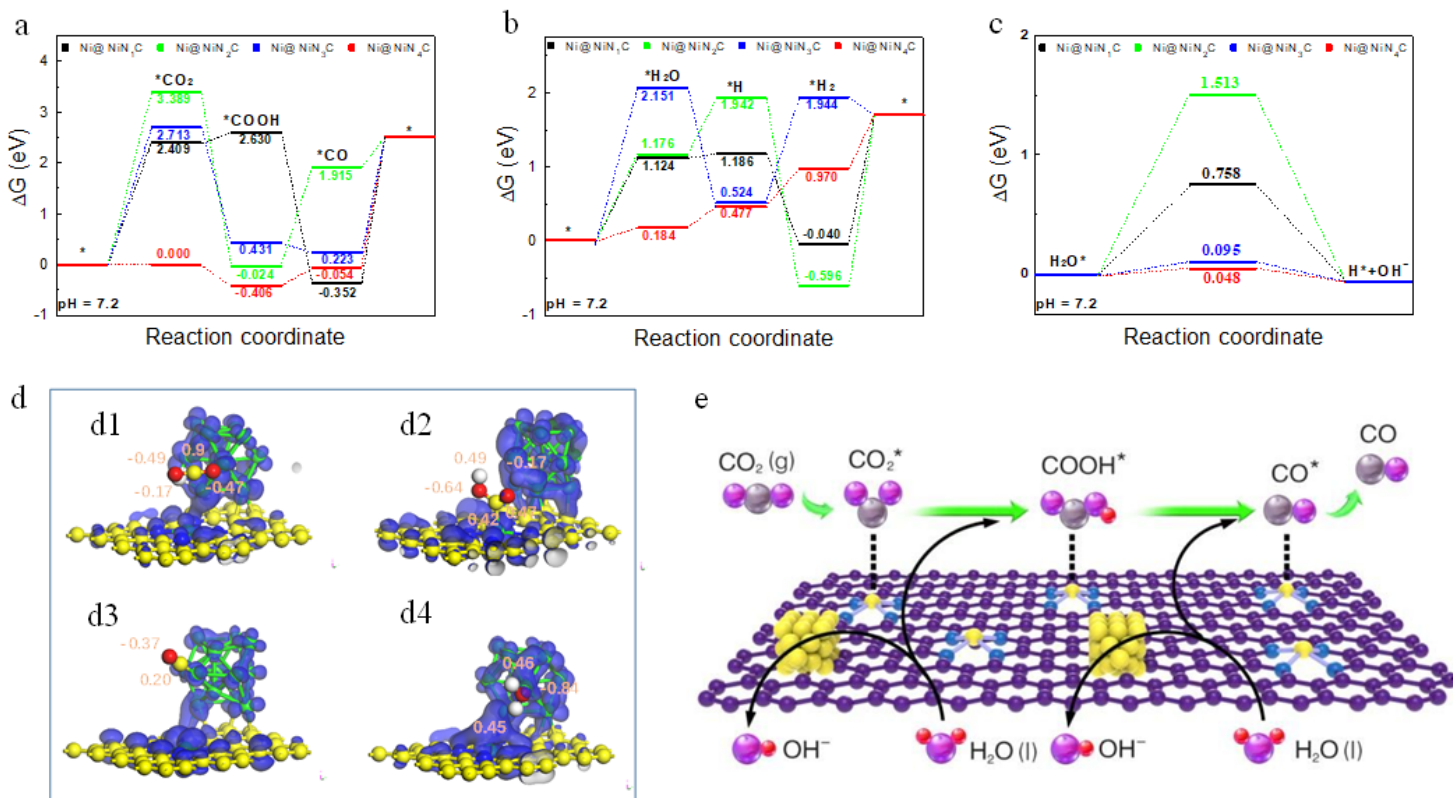


Figure 5

Theoretical calculations. DFT-based free energy profiles for the optimized Ni@NiN₁CM, Ni@NiN₂CM, Ni@NiN₃CM, and Ni@NiN₄CM models during the ECR a, HER b, and water dissociation process c. d, charge density of structural evolution of ECR for Ni@NiN₄CM (Ni: green, N: blue, O: red, H: white and C: yellow). e, A proposed reaction mechanism for the ECR to CO. Yellow, nickel; blue, nitrogen; pink, oxygen; grey, carbon; red, hydrogen.

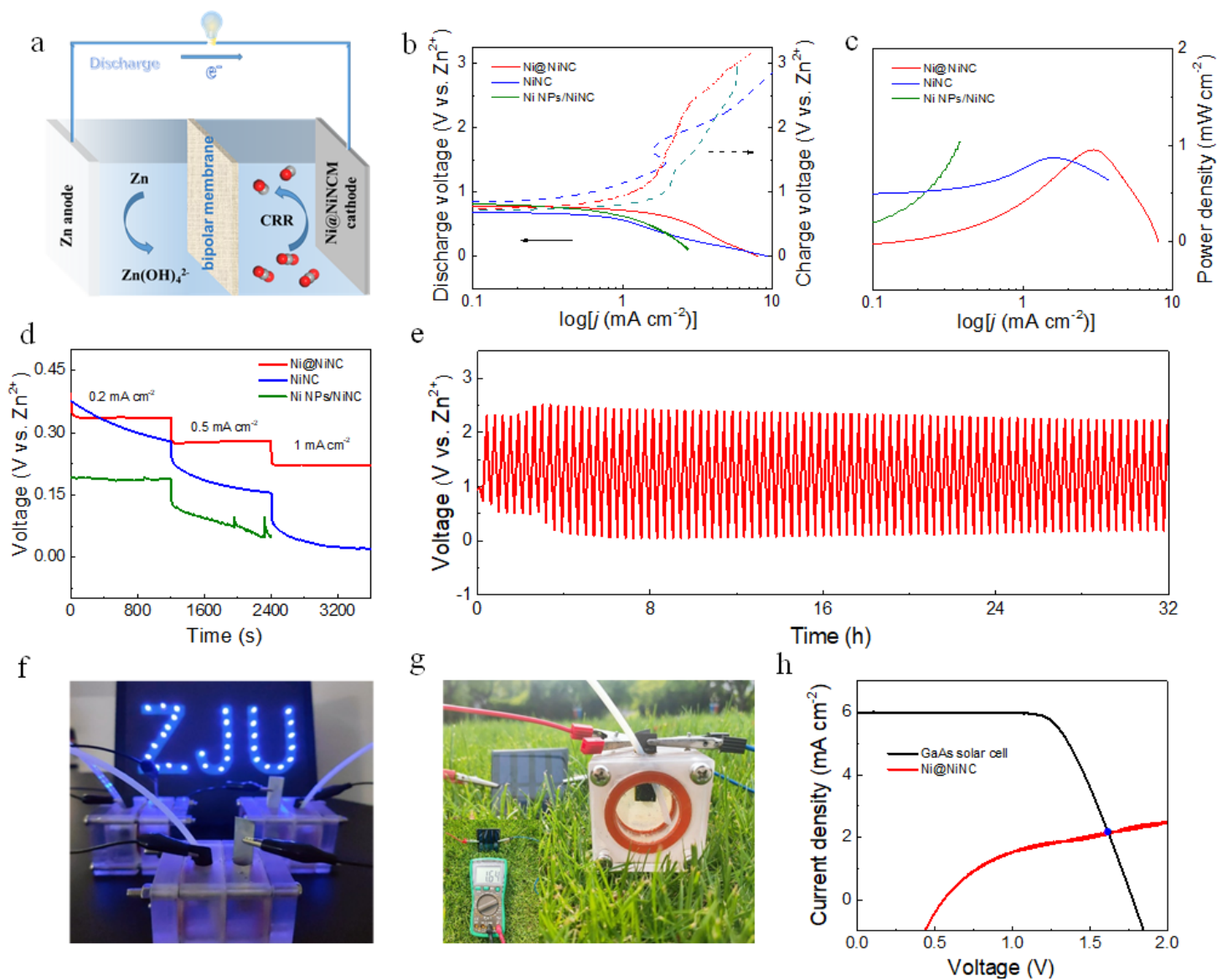


Figure 6

Zn-CO₂ battery. a, Schematic of developed Zn-CO₂ battery. b, Charge-discharge curves on Ni@NiNCM, NiNCM, and Ni NPs/NiNCM. c, Power densities of Ni@NiNCM, NiNCM, and Ni NPs/NiNCM. d, corresponding multiple current discharge curves at different discharging current densities. e, Discharge-charge cycling curve at 1.0 mA cm⁻² for 90 cycles, f, digital picture of Zn-CO₂ battery powered bulb glows. g, digital picture of GaAs solar cell for charging Zn-CO₂ battery. h, Photovoltaic current-voltage curves of the GaAs solar cell for charging Zn-CO₂ battery.

Supplementary Files

This is a list of supplementary files associated with this preprint. Click to download.

- SI090620LD.doc

- TOC.png